Surface etched carbon nanofiber companied ytterbium oxide for pinch level detection of fungicides carbendazim

Alagumalai Krishnapandi[a], Sivakumar Musuvadhi Babulal[b], Shen-Ming Chen[b]*, Selvakumar Palanisamy[d], Seong-Cheol Kim[a]*, Matteo Chiesa[c, d]*

[a] School of Chemical Engineering, Yeungnam University, Gyeongsan 38541, Republic of Korea.

[b] Department of Chemical Engineering and Biotechnology, College of Engineering, National Taipei University of Technology, No.1, Section 3, Chung-Hsiao East Road, Taipei 106, Taiwan.

[c] Department of Physics and Technology, UiT The Artic University of Norway, 9010, Tromso, Norway.

[d] Laboratory for Energy Laboratory for Energy and NanoScience (LENS), Khalifa University of Science and Technology, Masdar Campus, PO Box, 54224, Abu Dhabi, United Arab Emirates.

***Corresponding author**

Prof. Shen-Ming Chen, E-mail: smchen78@ms15.hinet.net

Prof. Seong-Cheol Kim, Email: sckim07@ynu.ac.kr

Prof. Matteo Chiesa, Email: matteo.chiesa@ku.ac.ae

Abstract

In the present work, we demonstrate for the first time the use of a ytterbium oxide nanorod/carbon nanofiber (Yb_2O_3/*f*-CNF) hybrid nanocomposite for the electrochemical detection of carbendazim (CBZ) fungicide. Various physicochemical methods such as Field Emission Scanning Electron Microscopy (FE-SEM), Transmission electron microscopy (TEM), and X-ray diffraction (XRD) spectroscopy have been used to confirm the formation of Yb_2O_3, *f*-CNF, and Yb_2O_3/*f*-CNF composite. Cyclic voltammetry and differential pulse voltammetry were employed to investigate different electrode electrochemical properties for the detection of CBZ. Compared with Yb_2O_3 and f-CNF, the Yb_2O_3/f-CNF nanocomposite exhibits the highest electrocatalytic activity toward the oxidation of CBZ. Under optimized conditions, the developed sensor shows a low detection limit (6 nM) and a wide linear range (50 nM to 3035 µM) with good sensitivity (0.2899 µA μM^{-1} cm^{-2}). Moreover, the fabricated sensor has demonstrated excellent stability, anti-interference ability, reproducibility, repeatability, and practicality. In addition, these sensor electrodes are easily prepared, affordable, portable, and effective at detecting CBZ fungicide residues in food and the environment.

Keywords: Yb_2O_3 nanorods; *f*-CNF; Nanocomposites; Carbendazim; Electrochemical sensor

1. Introduction

Globally, pesticide treatments during cultivation are gradually increasing to further the control and eradication of a variety of crop diseases [1], [2], [3]. Pesticide residues can be found in vegetables, fruits, processed food, water, air, and soil due to excessive and uncontrolled usage [4], [5], [6]. Carbendazim (methyl 2-benzimidazole carbamate, CBZ) is a harmful fungicide that belongs to the -IV family and is extensively used to eradicate weeds post-harvest and before planting seeds [7], [8], [9]. A stable benzimidazole ring makes CBZ resistant to environmental degradation. Moreover, the CBZ can persist in the environment for a long time, resulting in severe health problems and environmental risks [10], [11]. According to the Brazilian National Health Surveillance Agency (BANVISA) and China, 0.02-0.03 mg/kg of CBZ can be used in certain fruits like citrus fruits, apples, grapes, and bananas [12], [13]. On the other hand, the International Codex Alimentarius Commission (ICAC) recommends levels of CBZ varying from 0.05 to 20 mg kg^{-1} for crops [14][15]. However, CBZ traces can adversely affect humans, such as infertility, embryotoxicity, carcinogenic and mutagenic effects, testicular damage, and endocrine disruption [16]. The World Health Organization (WHO) has classified CBZ as a hazardous chemical because of its toxicity [17]. Even though CBZ has been banned in many countries (USA, Australia, Sweden, European Union), it is still used in cultivation due to its low prices and high yields [9]. Therefore, it is crucial to monitor CBZ levels accurately and rapidly in food products and water sources [18–20]. A variety of advanced analytical techniques have been used to detect CBZ in food and water to date, including chemiluminescence [21], high-performance liquid chromatography [22], Raman scattering [23], UV-Vis spectrometry [24], and electrochemical detection [15]. There are disadvantages to traditional chromatographic and spectrometric methods, such as their complex free treatment process, expansive instrumentation, inability to observe in

real-time, and long duration [25], [26]. In contrast, electrochemical methods have generated considerable attention due to their ease of operation, high accuracy, inexpensive equipment, quick response, and minimal chemical usage [27], [28]. Therefore, this study uses an electrochemical method to detect CBZ in food and water samples.

Lanthanide-based nanomaterials play a significant role in a variety of fields due to their unique properties such as unquenched magnetic moments, high magnetic susceptibilities, various oxidation states, electropositive properties, electronic relaxation times, partially filled semi-core 4f subshells, long excited-state lifetimes (>1 second), high dielectric constants, high resistivity, and large band gap energies [29]. Among them, lanthanide oxides have received sustained attention in diverse fields, such as catalysis, gas sensors, electrochemical sensors, temperature sensors, solar cells, and supercapacitors [30], [31]. They also have excellent mechanical, chemical, and thermal stability, high corrosion resistance, and low toxicity [32], [33], [34]. Ytterbium oxide (Yb_2O_3) nanomaterials have been chosen in this study because of their desirable catalytic properties, electrochemical redox properties, optical properties, and high electron transfer mediators on their surfaces. In addition, the high surface energies make them highly sensitive to the detection of targeted analytes [35], [36]. To date, Yb_2O_3 has been synthesized with different structures by many different methods, including hydrothermal [37], solution-doping technique [38], coprecipitation [39], sol-gel [40], electro-spinning [41], etc. However, the synthesized Yb_2O_3 nanoparticles have agglomerated on the electrode surface, reducing its efficiency during electrochemical analysis [42], [43]. It is possible to overcome these obstacles by using a chemically functionalized carbon nanofiber (*f*-CNF) substrate since carbonaceous nanomaterials are renowned candidates for electrode fabrication and can prevent agglomeration [33], [44]. It is worth noting that *f*-CNF has gained desirable properties, including considerable

mechanical strength, porosity, and uniformity of its surface. Additionally, its unique surface properties can enhance electron conductivity and electrochemical performance due to its cylindrical nanostructure and surface functional groups [45], [46], [47]. The hollow structure of the carbon nanofiber network structure facilitated molecular interaction, electrochemical activity on the electrode surface, and mechanical interlocking of the nanofibers facilitated electron transfer. Additionally, the *f*-CNF has a large surface area and appropriate pore size distribution, which make it a valuable candidate for electrochemical sensors [48], [49]. The combined nanocomposite of Yb_2O_3 with highly conducting properties and negative charge surfaces of *f*-CNFs can provide additional synergistic properties. Furthermore, the *f*-CNF enhances Yb_2O_3 electrocatalytic activity and allows its use in modified electrode materials for highly sensitive and selective detection of pesticides. [50], [51]. According to a literature survey, Yb_2O_3 nanoparticles modified carbonaceous electrodes were used for electrochemical determination of biological and hazardous molecules. For instance, Raja et al. [52] Ytterbium oxide/graphene oxide has been prepared with a green approach method, and a modified electrode was used to detect the 3-nitro-L-tyrosine. Mohammad et al. [32] RGO/ Yb_2O_3 NPs modified glassy carbon electrode for sensitive detection of metoclopramide in human fluids. Similarly, Carolina et al. used graphene/Yb_2O_3 composite-based carbon paste electrodes with good sensitivity and low detection limit (LOD) for the electrochemical detection of acetaminophen [53]. In the present study, Yb_2O_3 nanorods decorated with f-CNF (Yb_2O_3/*f*-CNF) hybrid composite-modified electrodes were prepared for selective and sensitive detection of toxic CBZ. In the literature, there are no sensor studies on CBZ that use either Yb_2O_3 or its composite so this study would draw the researcher's attention to CBZ's toxicity and detection mechanisms. In this study, we developed a novel electrochemical sensor using Yb_2O_3/*f*-CNF nanocomposite to detect CBZ in food and water samples (carrots, reddish water,

lake water, pond water). The sensor proposed in this study has a wider linear range and a lower LOD for the detection of CBZ. Additionally, real samples were analyzed to demonstrate the applicability of the developed CBZ sensor.

2. Materials and methods

2.1. Materials and reagents

Ytterbium acetate ($Yb(C_2H_4O_2)$, 99.9%), ammonium acetate ($C_2H_7NO_2$, 98%), and carbendazim (CBZ) were purchased from Sigma-Aldrich and used without further purification. Monosodium phosphate (NaH_2PO_4 (s), ≥99%) and disodium phosphate (Na_2HPO_4 (s), ≥98.5%) were used to make different concentrations supporting electrolyte solution during electrochemical analysis, and HCl and NaOH were used to adjust the pH value. Nitric acid (HNO_3) and sulfuric acid (H_2SO_4) were purchased from Sigma Aldrich. Potassium ferricyanide ($K_3Fe(CN)_6$ (s), ≥99%), potassium ferrocyanide ($K_4Fe(CN)_6$ (s), ≥99%), potassium chloride (KCl (s), >99%), sodium hydroxide (NaOH, >98%), and ethanol (CH_2OH (l), >98%) were purchased from Sigma-Aldrich.

2.2. Synthesis of Yb_2O_3 nanorods

A coprecipitation method was used to synthesize Yb_2O_3 nanorods. Initially, 0.1 M of $Yb(C_2H_4O_2)$ was dissolved in 50 mL of DI water and stirred continuously at room temperature. In addition, a few drops of ammonium acetate were gently added to the solution and continuously stirred for 2 hours at 350 rpm. A uniform, clean blue precipitate was obtained at the end of the reaction. The reaction mixture in the beaker was sonicated for 1 h for homogeneous formation andthe resulting residue was washed with deionized (DI) water and ethanol to remove any external impurities, then centrifuged at 400 rpm to remove any residual impurities. The precipitate was then dehydrated at 55°C for 24 h and calcined in a muffle furnace at 600 °C for 6 h.

2.3. Synthesis and fabrication of Yb_2O_3/*f*-CNF

To prepare the Yb_2O_3/*f*-CNF, 5 mg of as-prepared Yb_2O_3 and 2 mg of *f*-CNF were added to 1 mL of DI water. The composite suspension was kept under the ultrasonication bath until it reached a homogeneous suspension. The suspension was centrifuged for 15 minutes at 400 rpm to remove impurities and washed numerous times with DI water and ethanol. The attained Yb_2O_3/*f*-CNF composite was dried at 80 ℃ for 8 h. As expected, the presence of oxidized carboxylic functional groups of *f*-CNF holds on the wall to the Yb_2O_3 nanorod over the outer interlayers of the structure during ultrasonication. The overall synthesis process of Yb_2O_3/*f*-CNF is shown in **Scheme 1**. For the electrode preparation, about 5 µL of the above-prepared Yb_2O_3/*f*-CNF composite suspension was dropped on the glassy carbon electrode (GCE) and dried in an air oven. The fabricated Yb_2O_3/*f*-CNF composite electrode was utilized for further electrochemical nd catalytic studies. The same procedure was followed to prepare the other electrode.

2.4. Apparatus and measurements

The powder X-ray diffraction (XRD) patterns of the synthesized Yb_2O_3, *f*-CNF, and Yb_2O_3/f-CNF were measured by a PAN analytical X'Pert PRO diffractometer equipped with Cu Kα radiation (l = 1.5418 Å). The crystal structure of all samples was investigated from 10 to 90° 2θ with a step size of 0.02°. A JASCO FT-IR 460 Plus spectrophotometer was used to measure the IR spectrum of synthesized samples. The morphology, size, and surface features were examined using a High-resolution Transmission Electron Microscope (HR-TEM) and scanning images, selected area electron diffraction (SEAD), and elemental mapping was obtained using an HR-TEM: JEOL - 2100F. X-ray photoelectron spectroscopy (XPS, Thermo Scientific Multi-Lab 2000) was used to analyze the prepared samples' elemental composition and oxidation state. pH measurements were performed with a Horiba-L aqua pH meter calibrated with a standard buffer of the defined pH. All electrochemical experiments were carried out with a conventional three-electrode system equipped

with a modified GCE (3 mm diameter) as a working electrode, platinum wire as an auxiliary electrode, and Ag/AgCl (sat. KCl) as a reference electrode. The electrochemical studies were carried out using CHI 750A electrochemical workstation.

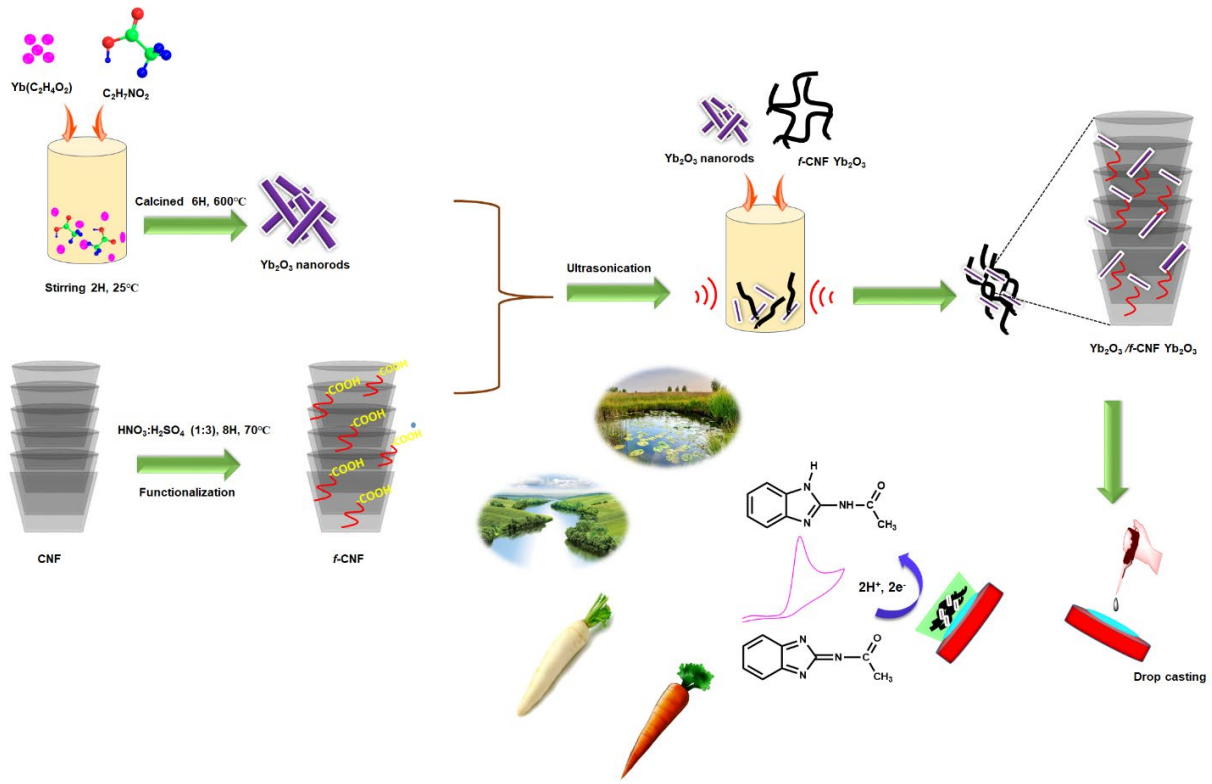

Scheme 1. Synthesis of individual Yb_2O_3 nanorods, *f*-CNF, and *f*-CNF/Yb_2O_3 composite and detection mechanism of CBZ in food and water samples.

3. Results and discussion

3.1. XRD and FTIR analysis

The crystal structure and phase purity of as-synthesized Yb_2O_3, *f*-CNF, and *f*-CNF/Yb_2O_3 composite were explored using XRD. The XRD pattern of Yb_2O_3 in **Fig. 1A** showed diffraction peaks at 2θ of 20.8°, 29.6°, 34.8°, 36.5°, 40.5°, 44.2°, 49.3, 58.6, and 61.5°, indicating lattice planes (211), (222), (400), (441), (332), (134), (440), (622) and (444), respectively, which are associated with BCC phase, space group-La_3 and well-matched with the previously reported

literature [JCPDS:0-0043-1037] [54]. The average crystalline size of Yb_2O_3 was calculated through 'Debye−Scherrer's equation'[55]:

$$D_{XRD} = K\lambda / \beta_{hkl} COS\theta \quad (1)$$

where λ is the wavelength of X-ray (0.15406 Å), D represents the size of crystallites (nm), θ is the diffraction angle, k is a constant value, and β is full with half maximum (FWHM) of the diffraction peak. The calculated average crystalline size (D) of the Yb_2O_3 was 19.08 nm. The lattice unit cell parameters were calculated as = 27.16 Å with a cell volume of 1136.59 Å. These results show that the synthesized Yb_2O_3 consists of only Yb and O, with no impurities detectable. The XRD pattern of the *f*-CNF is shown in **Fig. 1A**; the observed diffraction peaks at 24.4° and 42.2° were well indexed with (002) and (100), respectively, confirming the presence of carbon source [56]. Combining Yb_2O_3 with *f*-CNF resulted in lower metal oxide influence on the carbon surface because of the intensity of *f*-CNF.

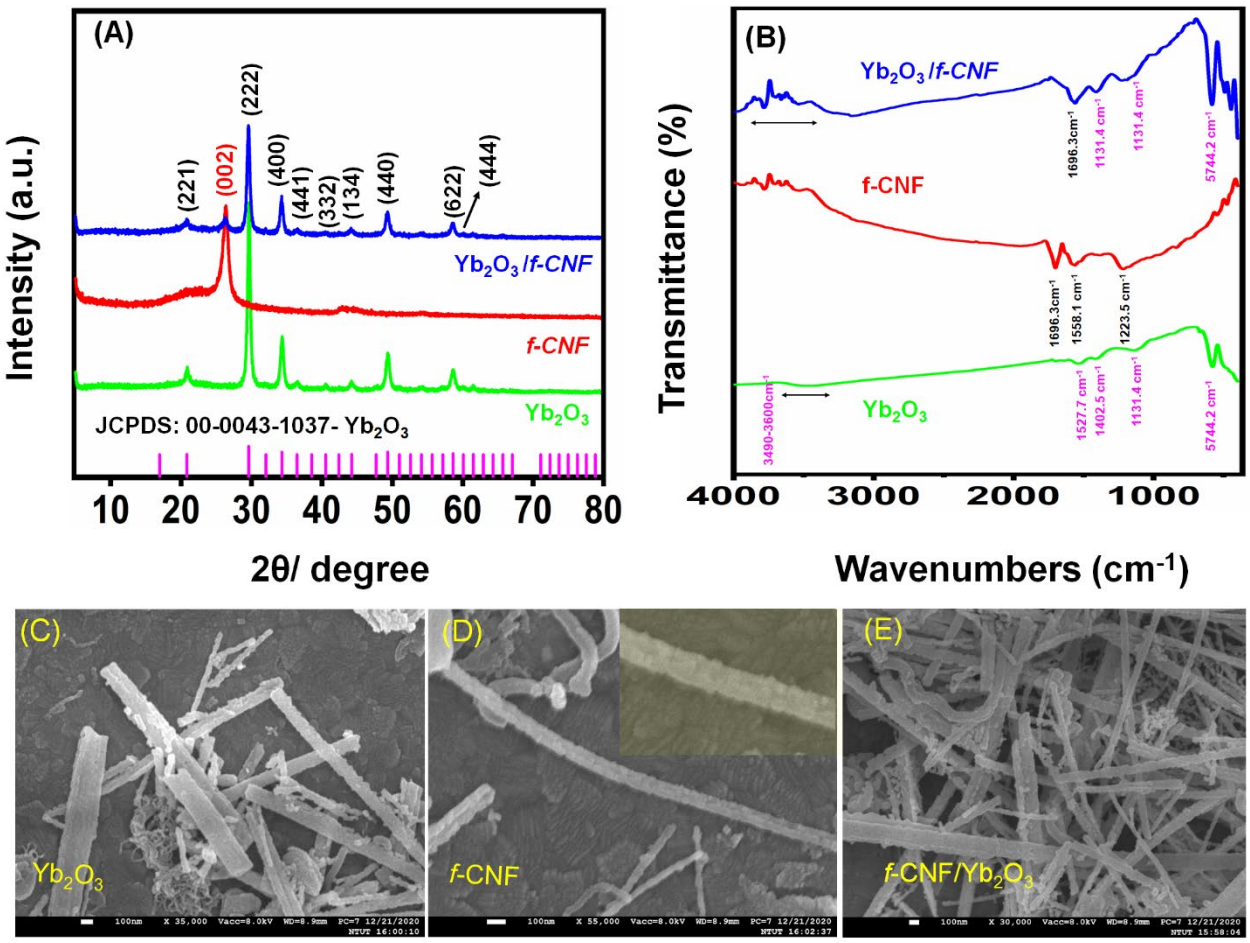

Fig. 1. (A) XRD and (B) FTIR spectrum of Yb_2O_3, *f*-CNF, and Yb_2O_3/*f*-CNF. FE-SEM images of Yb_2O_3 (C), *f*-CNF (D), and Yb_2O_3/*f*-CNF (E).

FTIR spectroscopy was used to find the functional groups of the as-prepared Yb_2O_3, *f*-CNF, and *f*-CNF/Yb_2O_3 nanocomposite. The FTIR spectrum of Yb_2O_3 showed a broad peak at 3490 – 3600 cm-1 corresponding to the adsorption of -OH stretching vibration, and three blend peaks noticed at 1131.4, 1402.5, and 1527.7 cm^{-1} are attributed to the CO_3^{2-} stretching vibration (**Fig. 1B**) [57]. A significant peak appears at 574.2 cm^{-1}, indicating the formation of Yb-O stretching vibration (metal-oxygen bond), which proves the formation of Yb_2O_3 nanoparticles [40][58]. The FTIR spectrum of *f*-CNF revealed sustainable peaks at 1223.5, 1558.1, 1696.3, 1701, and 3462 cm^{-1}, which belong to the acid-treated functional groups C-O, C=C, C=O, and -OH,

196 respectively [46][59]. Finally, all observed peaks appeared in the *f*-CNF/Yb_2O_3 nanocomposite
197 without any other impurities.

198 **3.2. Surface and structural analysis**

199 The surface structure, morphology, and size of Yb_2O_3, f-CNF, and Yb_2O_3/*f*-CNF were confirmed
200 using FE-SEM and HR-TEM studies. **Fig. 1C** shows a single nanorod structure morphology of
201 Yb_2O_3. It is possible for two-dimensional Yb_2O_3 nanorods to provide more active sites and more
202 electrode/electrolyte contact areas, and accelerate electron transfer activity at the electrochemical
203 reaction by their uniform surface morphology. **Fig. 1D** depicts the morphological features of
204 surface functionalized *f*-CNF, the one-dimensional hollow structure, and the rough surface caused
205 by the chemisorption of the organic substrate on the carbon surface after functionalization. As
206 shown in **Fig. 1E**, the ultrasonically fabricated composite of the Yb_2O_3/*f*-CNF revealed Yb_2O_3
207 fused to the surface of the *f*-CNF. Also, the HR-TEM images confirmed the individual structure
208 of Yb_2O_3 nanorods and *f*-CNF (**Fig. 2A** and **B**). From **Fig. 2A,** the diameter and length of Yb_2O_3
209 nanorods were calculated as 98 and 274 nm, respectively. The higher and lower magnification
210 TEM images of the composite reveals that the Yb_2O_3 nanorods are fused around the surface walls
211 of the *f*-CNF (**Fig. 2C** and **D**), which result from the strong attraction of chemically induced
212 oxygen functional groups (-COOH, -OH) by Yb_2O_3 nanorods. As shown in the HR-TEM image
213 of **Fig. 2E,** the d-spacings calculated for the Yb_2O_3 cubic crystal system (maximized in **Fig. 2F**)
214 were 0.331 and 0.143 nm, respectively, which is consistent with XRD results. The lattice fringes
215 of Yb_2O_3 are visible, indicating its high crystallinity, and *f*-CNF did not affect the crystallinity of
216 Yb_2O_3 nanorods in the nanocomposite (**Fig. 2F**). Based on the Energy-dispersive X-ray (EDX)
217 analysis (**Fig. S1A**), the percentages of the elements were determined as Yb (61.1%), O (7.44%),

and Yb (31.18%). Additionally, the elemental mapping images of **S1. B-C** reveals Yb, O, and C in the Yb_2O_3/*f*-CNF composite.

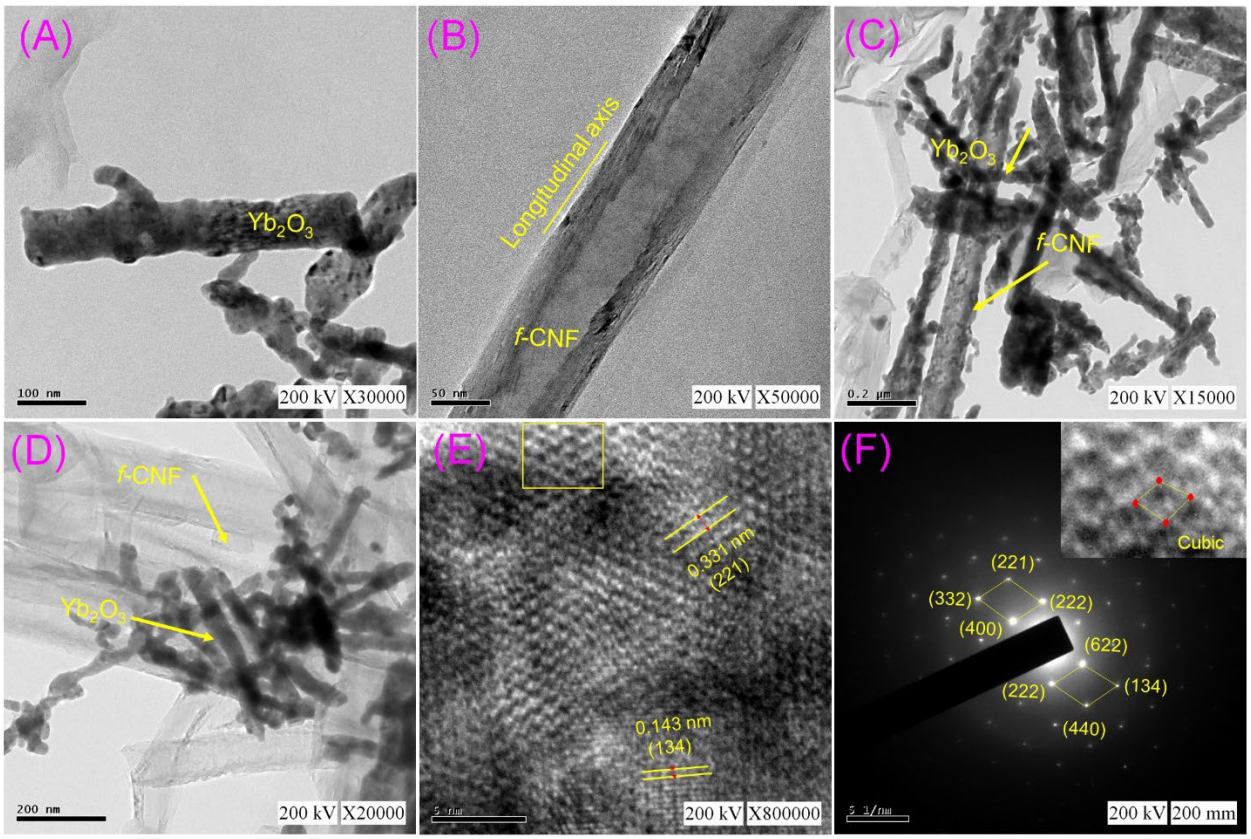

Fig. 2. TEM images of (A) Yb_2O_3, (B) *f*-CNF, (C and D) Yb_2O_3/*f*-CNF, and (E) Lattice fringe and (F) SEAD pattern of Yb_2O_3.

3.3. XPS analysis

The chemical composition and oxidation state of Yb_2O_3/*f*-CNF nanocomposite are revealed by XPS. The overall scanning survey spectra (**Fig. 3A**) of Yb_2O_3 peaks observed at 236.1 eV (Yb 4d), 533.2 eV (O1s), and f-CNF at 282.5 eV (C 1s), 532.1 eV (O 1s), respectively. The Yb_2O_3/*f*-CNF nanocomposite shown in **Fig. 3A**, which exhibits the presence of Yb 4d, C1s, and O1s, is located at 189.6, 285.6, 533.2 eV, respectively, with minor distortion on the position. **Fig. 3B** shows the Yb 4d XPS spectrum of Yb_2O_3 at 188.5 eV, which corresponds to Yb^{3+} [60][61], and in Yb_2O_3/*f*-

CNF nanocomposite, the peak moved around +1.2 eV due to carbon-metal interactions. The individual C1s spectrum in **Fig. 3C** contains the four different oxygen peaks with binding energies at 290.2, 286.3, 284.8, and 284.3 eV. These are relevant to the functional groups CO_2H, C=O/C-O, and C-C and C=C, respectively. The same peaks were also obtained on Yb_2O_3/*f*-CNF nanocomposite with +0.21 eV positive shift and reduced from the original intensity [62], [63]. In Fig. 3D, the two significant O1s peaks are attributed to lattice oxygen (534.0 eV) and metal-oxygen bond (531.3 eV) on Yb_2O_3. The *f*-CNF showed three significant peaks at 531.2, 532.5, and 534.2 eV, which correspond to the oxygen double bond (O=C-O/COO-), a hydroxyl group (C-OH) or C-O functional group, and oxygen single bond (O=C-O), respectively. The intensity of these peaks was reduced due to metal attracted to the oxygen functional groups [62][64]. As a result of the combination of Yb_2O_3/*f*-CNF nanocomposite, there are more active sites for electrochemical reactions, which enhances electrocatalytic activity.

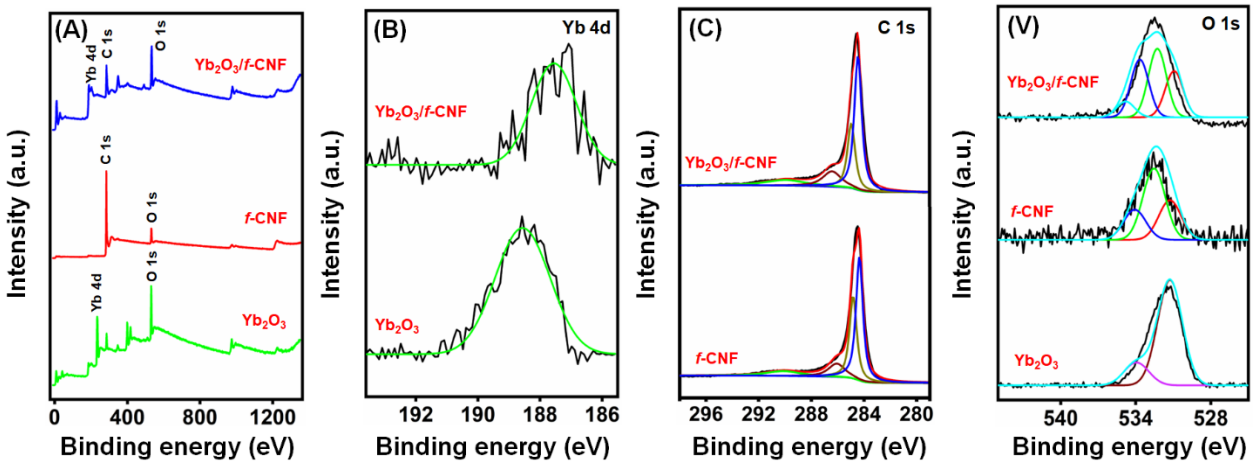

Fig. 3. The overall survey spectra for Yb_2O_3, *f*-CNF, and Yb_2O_3/*f*-CNF nanocomposite. Individual high-resolution XPS spectra of (A) Yb 4d, (B) C1s, and (C) O 1s.

4. Electrochemical analysis

4.1. Electrocatalytic performance of the modified electrode

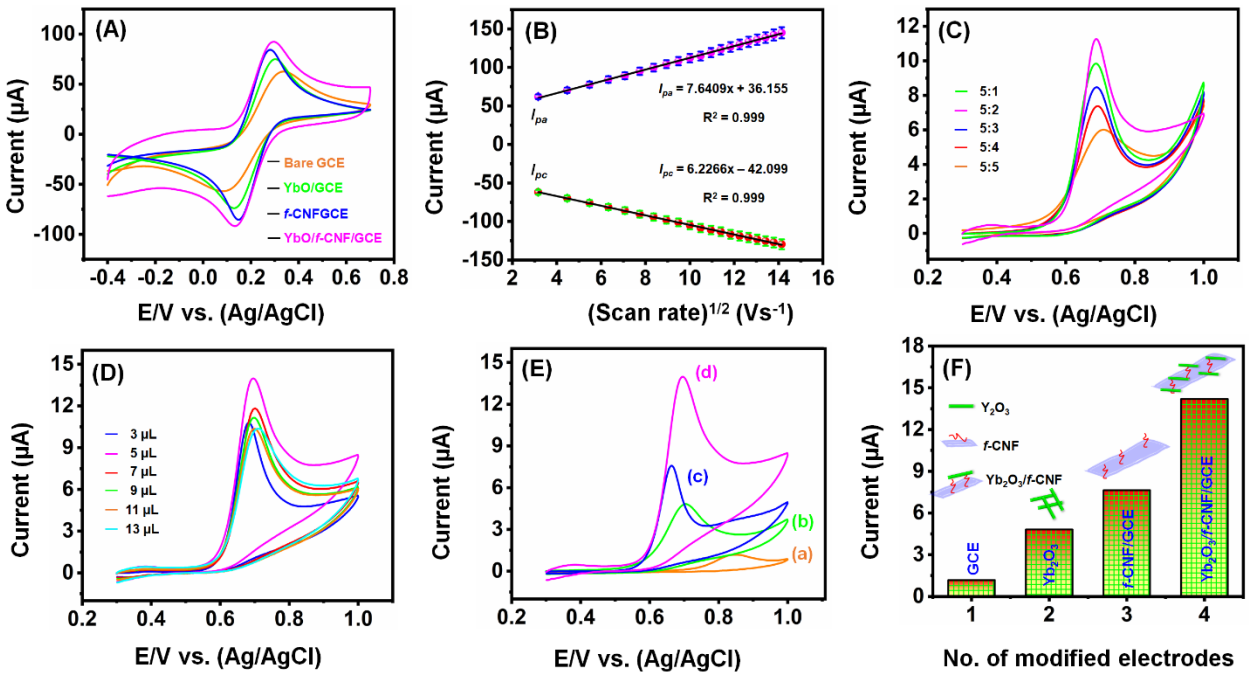

Fig. 4. (A) CV response of bare GCE, Yb_2O_3/GCE, *f*-CNF/GCE, and Yb_2O_3/*f*-CNF/GCE in 5 mM of $[Fe(CN)6]^{3-/4-}$ comprises of 0.1 M of KCl at a scan rate of 50 mVs^{-1}, (B) The linear relationship between the square root of scan rate (mVs^{-1}) *vs.* anodic and cathodic peak current (I_{pa} and I_{pc}). (C) Different ratios of catalyst optimized in the presence of 200 µM CBZ. (D) Various loading amounts of catalyst optimized in the presence of 300 µM CBZ (E) CV curves of different electrodes at scan rate 50 mVs^{-1} presence of 300 µM CBZ, (F) Bar chart of different individual electrodes current response for the detection of 300 µM CBZ.

The electron transfer and electroactive surface area of the different electrodes were evaluated by performing CV. The electrochemical performance of modified and unmodified electrodes was carried out in a mixed solution of 5 mM $[Fe(CN)_6]^{3-/4-}$ and 0.1 M KCl. **Fig. 4A** showed that redox peak intensities of the bare GCE display a weak redox peak response due to weak electron transfer. When GCE was modified with Yb_2O_3/GCE, *f*-CNF/GCE, and Yb_2O_3/*f*-CNF/GCE, its electrochemical performance gradually increased in the redox peak current of Fe^{II}/Fe^{III}. The redox peak current for Yb_2O_3/*f*-CNF/GCE was more significant than those of other

electrodes, implying that the Yb_2O_3 interacts with a strong π-π bond on *f*-CNF, which may contribute to the higher electrocatalytic activity and electron transfer kinetics of Yb_2O_3/*f*-CNF/GCE. Additionally, the electroactive surface area of the unmodified and modified electrodes was determined using CV in a mixed solution of 5 mM $[Fe(CN)_6]^{3-/4-}$ and 0.1 M KCl solution at different scan rates (10-200 mVs^{-1}), as shown in **Fig. 4B**. The Rendles-Sevick Eqn. (1) [65] was used to calculate the active surface area of the Yb_2O_3/GCE, *f*-CNF/GCE, and Yb_2O_3/ *f*-CNF/GCE, and was found to be 0.081, 0.090, and 0.99 cm^2, respectively.

$$I_p = 2.69 \times 10^5 \; An^{3/2} \; D^{1/2} \, \text{red C} \times V^{1/2} \qquad (1)$$

Where I_p is the redox peak current (μA), A is the electroactive surface area (cm^2), D is the diffusion coefficient (7.6 x 10^{-6}), n is the number of electrons (n=1), and v is the scan rate (Vs^{-1}). Finally, Yb_2O_3/*f*-CNF/GCE possesses the most electroactive surface area among the other electrodes. Hence, the large surface area of the nanocomposite offers the robust channeling of an electron across the interphase and enhances electrocatalytic performance.

4.2. Optimization of conditions

In order to optimize the Yb_2O_3/*f*-CNF for electrode modifications, the different weights of *f*-CNF containing Yb_2O_3 composite dispersions were prepared using DI water. The resulting composite drop-coated modified electrodes were analyzed for detection of CBZ (200 μM) at a scan rate of 50 mVs^{-1}. **Fig. 4C** shows the CV response of Yb_2O_3 with different ratios of *f*-CNF (5:1, 5:2, 5:3, 5:4, 5:5) in which the amount of Yb_2O_3 kept as 5 mg/mL. It can be seen that the CBZ oxidation peak current gradually increased upon increasing the amount of *f*-CNF with Yb_2O_3, and the peak current of CBZ was degreased over 2 mg/mL of *f*-CNF. A thick layer of *f*-CNF may prevent CBZ molecules from accessing binding sites because of excess amounts of *f*-CNF. A 5:2 mg ratio of the electrode modifier was found to produce the maximum peak current, so this ratio

was chosen for electrode modification. Then, the different casting amounts of above-optimized Yb_2O_3/*f*-CNF were examined using CV, and the obtained results are shown in **Fig. 4D**. The CBZ oxidation peak current increased remarkably when the catalyst loading was increased. The significant oxidation peak current response of CBZ was observed for the 5 µL suspension drop-coated composite electrode. Thus, the above-optimized ratio and drop coating amount of Yb_2O_3/*f*-CNF were used for the entire electrochemical experiment.

The electrochemical response of CBZ (200 µM) at different electrodes was investigated by CV in pH 7.0 at a scan rate of 50 mV s^{-1} with a broad oxidation peak potential (E_{pa}) window (0.3 to 1.0 V). In GCE, a low oxidation peak current (I_{pa}) and high oxidation potential (0.83V) was noticed due to the slower electron transfer of bare GCE. Oxidation peak current and peak potential in the other electrodes gradually increased. The modified electrodes are arranged in increasing order of Yb_2O_3/GCE (I_{pa}=4.8 µA, E_{pa} = 0.70 V)>*f*-CNF/GCE (I_{pa}=7.6 µA, E_{pa} = 0.66 V)> Yb_2O_3/*f*-CNF/GCE (I_{pa}=13.9 µA, E_{pa} = 0.69 V), as shown in **Fig. 4E** and **4F**. Yb_2O_3/*f*-CNF/GCE exhibited a higher oxidation peak current and lower peak potential due to the synergetic effect of Yb_2O_3 nanorods and *f*-CNF. The synergetic effect of Yb_2O_3/*f*-CNF composite results in the enhanced electron transfer between the electrode surface and analyte (CBZ) than bare, Yb_2O_3, and *f*-CNF modified GCEs. Moreover, Yb_2O_3 over the surface of *f*-CNF bonded through π-π interaction, and its synergistic effect improved the electrocatalytic activity toward the CBZ oxidation. No reduction peak was attained during the reverse scan, which proved the irreversible reaction process and only happening oxidation on the modified electrode surface. Besides, the anodic peak represents the oxidation of the double bond of carbamate in carbendazim to form an amide and heterocyclic radical. Likewise, the oxidation of CBZ on the Yb_2O_3/*f*-CNF/GCE surface involves two electrons and two protons (**Scheme 2**).

4.3. CBZ concentrations and scan rates

The effect of various scan rates was investigated in the range from 10 – 100 mVs^{-1} for CBZ (200 µM) detection at Yb_2O_3/*f*-CNF/GCE in pH 7.0. The I_{pa} of CBZ increased gradually with the increasing scan rates, and the peak current was proportional to the scan rate in the potential range (**Fig. 5A**). In **Fig. 5B,** the relationship plot between scan rates (mVs^{-1}) and I_{pa} was described by the equation of I_{pa} = 0.0927v + 6.9951 (R^2=0.991). Also, the linear relationship expressed for the I_{pa} *vs.* square root of scan rate (mVs^{-1}) equation is I_{pa} = 0.0706v (mVs^{-1}) + 3.1377 (R^2 = 0.98), which suggests that the electrochemical reaction of CBZ at Yb_2O_3/*f*-CNF/GCE followed the surface adsorption-controlled process. The linear relationship of E_{pa} vs. log scan rates expressed in the linear equation is E_{pa} (V) = 0.5839 – 0.5632 (R^2=0.999). The Bulter-Volumer Eqn. (2) [65] was used to calculate the number of electrons participating in the electrochemical reaction during the CBZ oxidation at Yb_2O_3/*f*-CNF/GCE.

$$E_{pa} = E° - \left(\frac{RT}{\propto nF}\right) l_n \left(RT \frac{K_s}{\propto nF}\right) + \left(\frac{RT}{2} \propto nF\right) l_n v \quad (2)$$

Where $E°$ is the standard potential, ∝ is the electron transfer coefficient, R is the gas constant, T is the surrounding temperature, F is the Faraday constant, and v is the scan rate. The value of $\propto n$ is 1.03, calculated from the obtained slope value of 0.5632, and the value of ∝ is 0.5. The calculated value is 1.98 and is close to 2; thus, two protons and two electrons participated during the CBZ oxidation at Yb_2O_3/*f*-CNF/GCE [69], [70].

The CBZ was quantitatively determined through voltammograms obtained with CV at various concentration range from 50 to 400 µM at a scan rate of 50 mVs^{-1}, as shown in **Fig. 5C**. When the concentration of CBZ increased linearly, the oxidation peak current also increased equally without change its oxidation potential (0.69 V). This indicates the high stability of the electrode at high concentrations, with more readily available active sites. In **Fig. 5D,** the oxidation peak current and

various concentration of CBZ expressed in the linear regression equation as I_{pa} = 0.0388$_{CPZ}$ + 2.6571(R^2 = 0.991). These results indicate the excellent kinetics and higher electrocatalytic activity of Yb_2O_3/*f*-CNF/GCE towards CBZ.

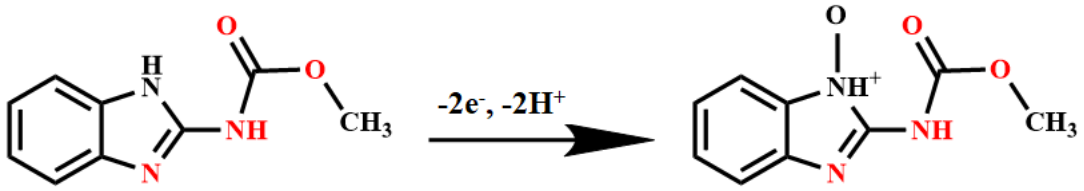

Scheme 2. The possible electrochemical oxidation of CBZ on Yb_2O_3/*f*-CNF/GCE.

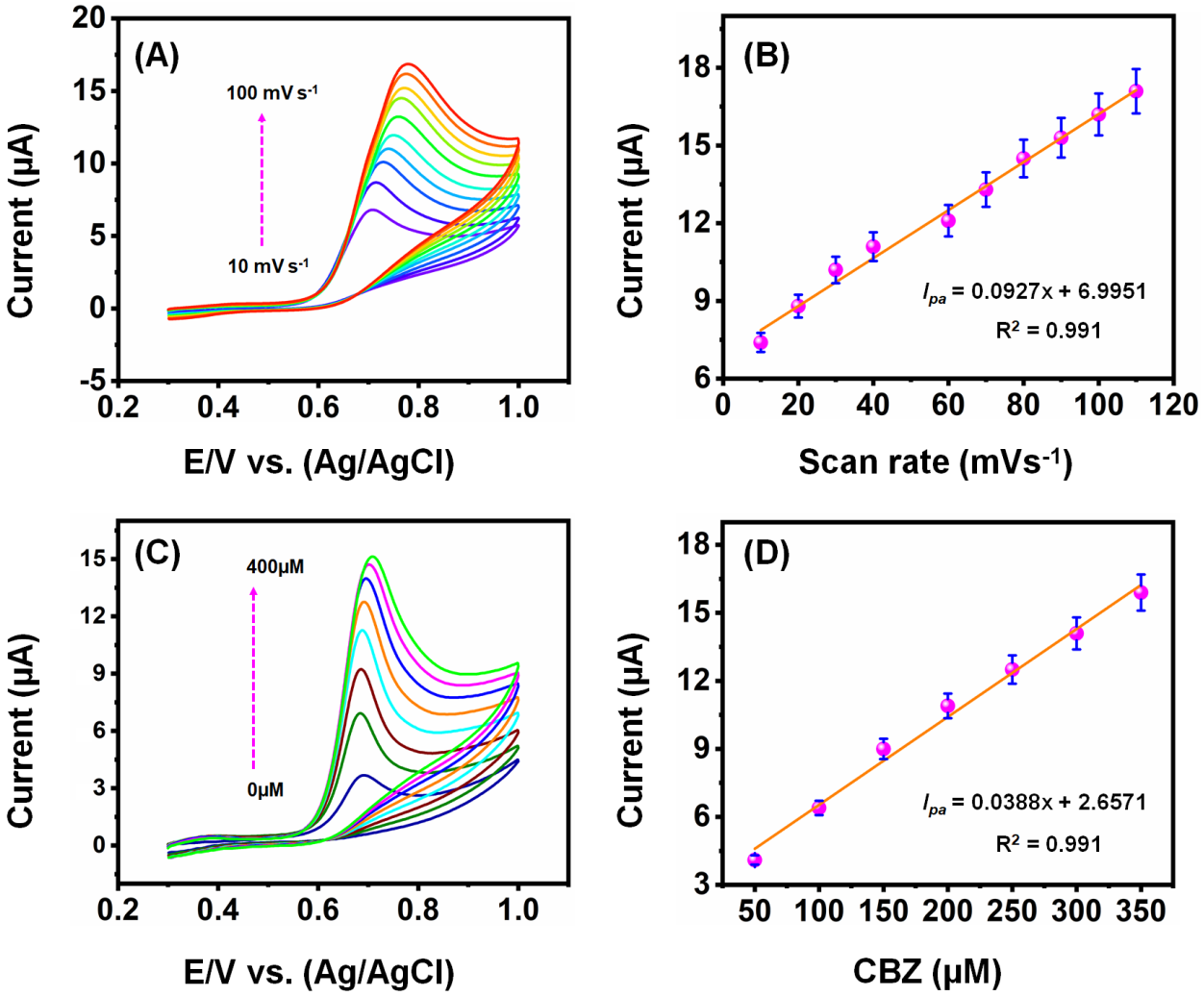

Fig. 5. (A) CV response of CBZ (200 μM) at Yb_2O_3/*f*-CNF/GCE with different scan rates (10–100 mVs^{-1}). (B) The linear relationship between the different scan rates *vs.* I_{pa}. (C) CV response for

different concentrations addition of CBZ (0-400 µM) at Yb_2O_3/*f*-CNF/GCE at a scan rate of 50 mVs^{-1}. (D) The linear relationship between the [CBZ] *vs.* I_{pa}.

4.4. Influence of pH

The pH for CBZ sensing at Yb_2O_3/*f*-CNF/GCE was investigated using different pHs from 3.0 – 11.0 at a scan rate of 50 mVs^{-1} (**Fig. 6A**). The I_{pa} and E_{pa} of CBZ have been moved towards the negative region when varying the pH of an electrolyte from the low to high, suggesting that the protons are taking part in the electrode reaction process. The maximum oxidation current of CBZ was observed at pH 7.0 and was selected as the optimal pH for this study. In **Fig. 6B** revealed the relationship between the different pH *vs.* E_{pa} can be found as E_{pa} (V) = -0.054 pH + 0.829 (R^2 = 0.994). The obtained slop value of 54 mV/pH was compared with the Nernst theoretical value (**Eqn. 3**). The obtained value is close to the theoretical value of 59 mV/pH, indicating the equal ratio (m/n=1) of electron and proton ($2e^-$ and $2H^+$) involved in the electrochemical reaction of CBZ oxidation.

$$E_{pa} = E° - \left(\frac{2.303mRT}{nF}\right) pH = E° - 0.059\frac{m}{n} pH \quad (3)$$

4.5. Determination of CBZ on Yb_2O_3/*f*-CNF/GCE

DPV is an ideal electrochemical method for the electrochemical determination of various analytes due to its higher sensitivity, lower detection limit, and lower background current response [66–68]. Therefore, the response current of CBZ at the Yb_2O_3/*f*-CNF/GCE sensor was explored through the DPV curves in the CBZ concentration range of 50 nM to 3035 µM (**Fig. 6C**). Under the optimized condition, the response current of CBZ presents a significantly enhanced trend with the increase of CBZ concentration. The two linear curves are plotted at low and high concentrations of CBZ. The first linear equation is expressed as I_{pa} (µA) = $0.049C_{CBZ}$ +0.3719 (R^2 = 0.993) in the CBZ concentration range of 50 nM-155 µM, as seen in **Fig. 6D**. Second equation is expressed as

I_{pa} (μA) = 0.0078C_{CBZ} + 10.227 (R^2 = 0.993) in the CBZ concentration range of 156-3035 μM. As a result of the consecutive linear range, when injecting CBZ, the molecules rapidly bind to the electrode surface because free active sites are initially unused. As concentration increases, CBZ curves shift toward a more positive region with a low oxidation current. The oxidation of CBZ at modified Yb_2O_3/*f*-CNF/GCE surfaces is comparatively slow since there are fewer unoccupied active sides. It was revealed that the occupied sites had a low electroactive area and sensitivity. Therefore, the first linear equation is used to calculate the low detection limit (LOD) by Eqn. (4) [66, 67].

$$LOD = 3S_b/S \quad (4)$$

Where Sb is the standard deviation of the blank signal (S_b=3), and S is the slope value of the primary linear range. The calculated LOD is 6 nM, and the sensitivity is 0.2899 μA μM^{-1} cm^{-2} (Sensitivity = slope value of the curve/surface area of Yb_2O_3/*f*-CNF//GCE), respectively. From this experiment, the obtained results were compared with previously reported literature. The Yb_2O_3/*f*-CNF/GCE sensor displayed a better LOD, sensitivity, and wide linear range than previously reported many CBZ sensors, as shown in **Table 1**.

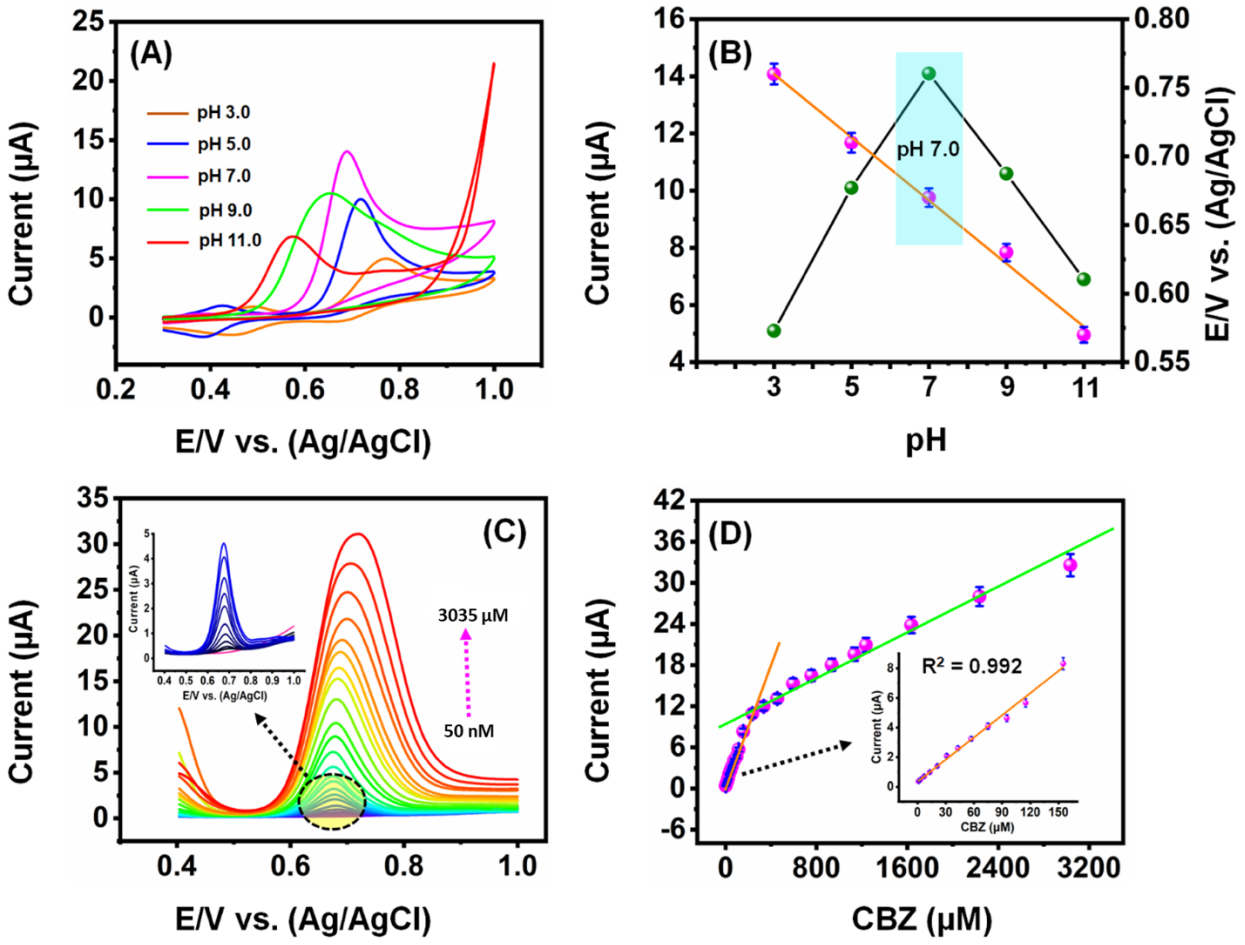

377

378 **Fig. 6.** (A) CV response of Yb_2O_3/*f*-CNF/GCE for CBZ (300 μM) in different pH (pH 3.0 – 7.0)
379 at scan rate 50 mVs^{-1}. (B) The linear relationship between the pH *vs.* I_{pa} and E_{pa}. (C) DPV response
380 of the Yb_2O_3/*f*-CNF/GCE for successive addition of CBZ from 50 nM to 3035 μM. (D) The linear
381 relationship between the CBZ concentrations (μM) *vs.* current response.

382 **Table 1.** Comparison of sensing performance of the fabricated CBZ sensor with previously
383 reported various CBZ sensors.

Electrode	Method	Linear range (μM)	Limit of detection (nM)	Refs.
$ZnFe_2O_4$/SWCNT/GCE[a]	DPV[c]	0.5-100	90	[71]
SiO_2/MWCNT/GCE[a]	SWV[d]	0.2-4.0	56	[72]
$Ti_3C_2T_x$MXene/GCE[a]	DPV[c]	0.05-100	10.3	[73]

P-HCNFs/GCE[a]	DPV[c]	1-35	38	[74]
NP-Cu/RGO/GCE[a]	DPV[c]	0.5-30	90	[75]
La-Nd_2O_3/CPE[b]	DPV[c]	0.08-50	27	[76]
D-PC/GCE[a]	SWV[d]	0.01-1.00	6	[7]
Ce-dope $ZnWO_4$/GCE[a]	DPV[c]	0.01-5.5	3	[77]
$WO_{3.0}.33H_2$/GCE[a]	SWV[d]	0.1-250	22	[78]
Fe-CuV/GCE[a]	DPV[c]	0.01-83.1	5	[79]
MBC@CTS/GCE[a]	DPV[c]	0.1-20	20	[22]
QD-rGO/CPE[a]	DPV[c]	0.1-11.8	91.6	[80]
TCP/CPE[a]	DPV[c]	0.5-10	300	[81]
MWCNTs/GCE[a]	SWV[d]	0.256-3.11	54.9	[82]
Yb_2O_3/f-CNF/GCE[a]	DPV[c]	0.05-155 156-3035	6	This work

[a]GCE-Glassy carbon electrode, [b]CPE-Carbon paste electrode, [c]DPV- Differential pulse voltammetry, [d]SWV- Square wave voltammetry,

4.6. Selectivity, reproducibility, repeatability, and storage stability

It is essential to ensure the electrode's selectivity to use it effectively for practical applications. As shown in **Fig. 7A**, the Yb_2O_3/*f*-CNF/GCE response current for CBZ (at 50 mVs^{-1} scan rate**)** was not affected in the presence of excessive amounts of interfering compounds (like pesticides, biological compounds, and metal ions, including amatryn, parathion, thiamethoxam, 2,4,6-trichlorophenol, carbofuran, calcium, potassium, magnesium, iron, aluminum, copper, chlorine, and sulfate). The RSD was calculated as 3.66 ± 0.158. The above result confirms the highly selective nature of Yb_2O_3/*f*-CNF/GCE toward CBZ. The relative error bar is shown in **Fig. 7B.** The obtained results suggest that the CBZ oxidation peak current was not affected by the presence of the above-mentioned interfering species. Hence, the fabricated sensor electrode can be used for real-time CBZ monitoring. The reproducibility, repeatability, and storage stability of the modified Yb_2O_3/*f*-CNF/GCE sensor were examined for the detection of CBZ (50 µM). Eight different Yb2O3/f-CNF/GCEs were prepared and evolved using DPV (Fig. 7C-D) for the

reproducibility studies. The current response of the eight different electrodes had the same potential as the peak current of CBZ. From these DPV curves, the calculated RSD was 4.51 ± 0.51. Then repeatability of the Yb_2O_3/*f*-CNF/GCE sensor was evaluated with the same experimental conditions as mentioned above (**Fig. 7E**). In this experiment, 26 cycles were continuously operated, and RSD was calculated as 4.77 ± 2.63. Even after 26 cycles, the CBZ oxidation peak current was retained (-0.4 µA) from the initial value, indicating the high repeatability of the sensor. In addition, the long-term stability (**Fig. 7F**) of the modified Yb_2O_3/*f*-CNF/GCE was examined at intervals of 4 days, with theelectrode stored in a refrigerator at 4°C when not in use, for detection of CBZ (50 µM, 0.01M). The peak current value is still 96% of the original value (maximized in **Fig. 7F**) after 36 days, proving the electrode's long-term stability. According to the above results, the modified Yb_2O_3/*f*-CNF/GCE sensor was reproducible, repeatable, and stable toward the detection of CBZ.

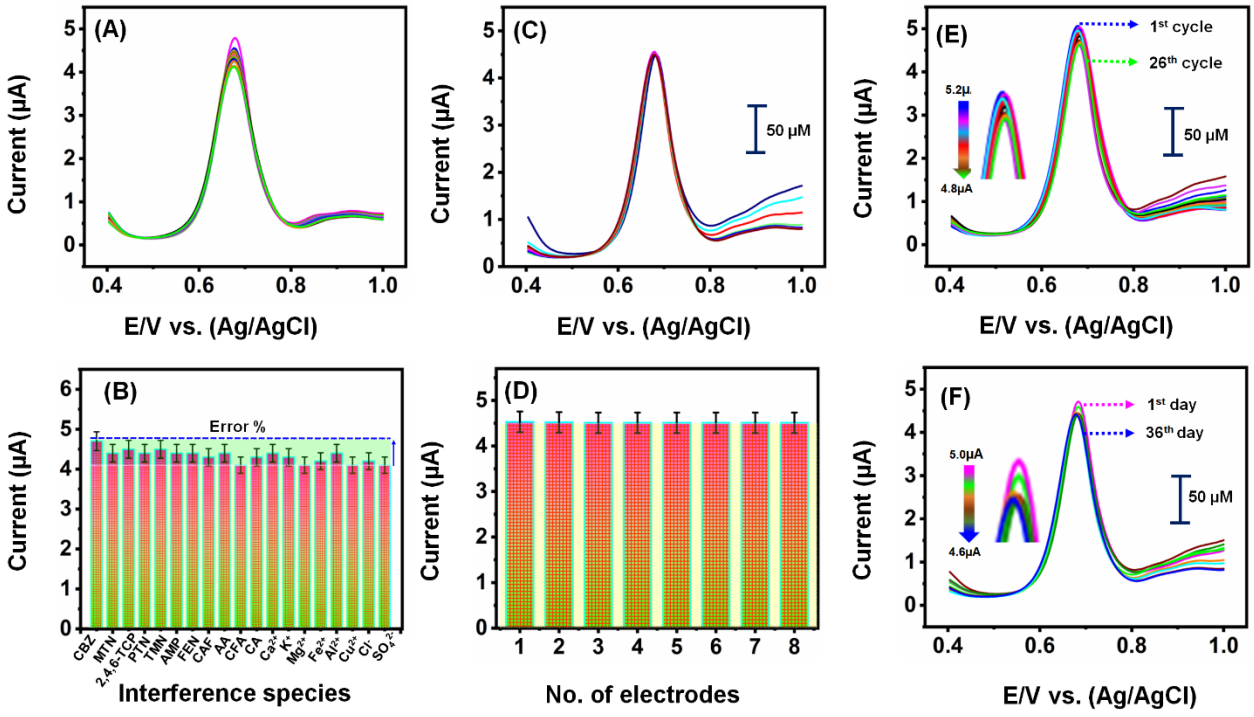

Fig. 7. (A-B) Selectivity & error bar diagram, (C-D) Reproducibility & bar diagram, (E) Repeatability, and (F) Long-term stability of Yb_2O_3/*f*-CNF/GCE toward CBZ.

4.7. Real-time application

The real-time detection capability of the proposed CBZ sensor has been evaluated in food and the environment to use it in practical applications. The real samples of carrot, radish, lake water, and pond water were used to evaluate the practical feasibility of the Yb2O3/f-CNF composite. The vegetables were purchased from a local market in Taiwan. The vegetable samples were peeled, cut into small pieces, and crushed with an electric blender before analysis. After collecting the extract, it was centrifuged for 15 minutes at 3000 rpm. First, the 1 mL of separated supernatant extract was diluted with 9 mL DI water. The pH was adjusted to pH 7.0. The real samples in the absence and presence of different concentrations of CBZ were studied using DPV. The obtained results are shown in **Fig. 8A-D**. It can be seen that the carrot (A), radish (B), lake water (C), and pond water (D) real samples did not show any DPV response in the absence of CBZ, which indicates that these real samples are CBZ-free. A sharp DPV response was observed for real samples containing CBZ (5 µM), and the DPV response current increased with an increasing CBZ concentration (10, 15, and 20 µM). The standard addition method was used to calculate the recovery of CBZ in the real sample, and the obtained recovery values are listed in **Table 2**. The recovery rate of the sensor ranged from 96.0% to 99.4%, with an acceptable relative standard deviation (RSD). According to the above results, the detection method based on the Yb2O3/f-CNF composite electrode can be used to determine CBZ presence.

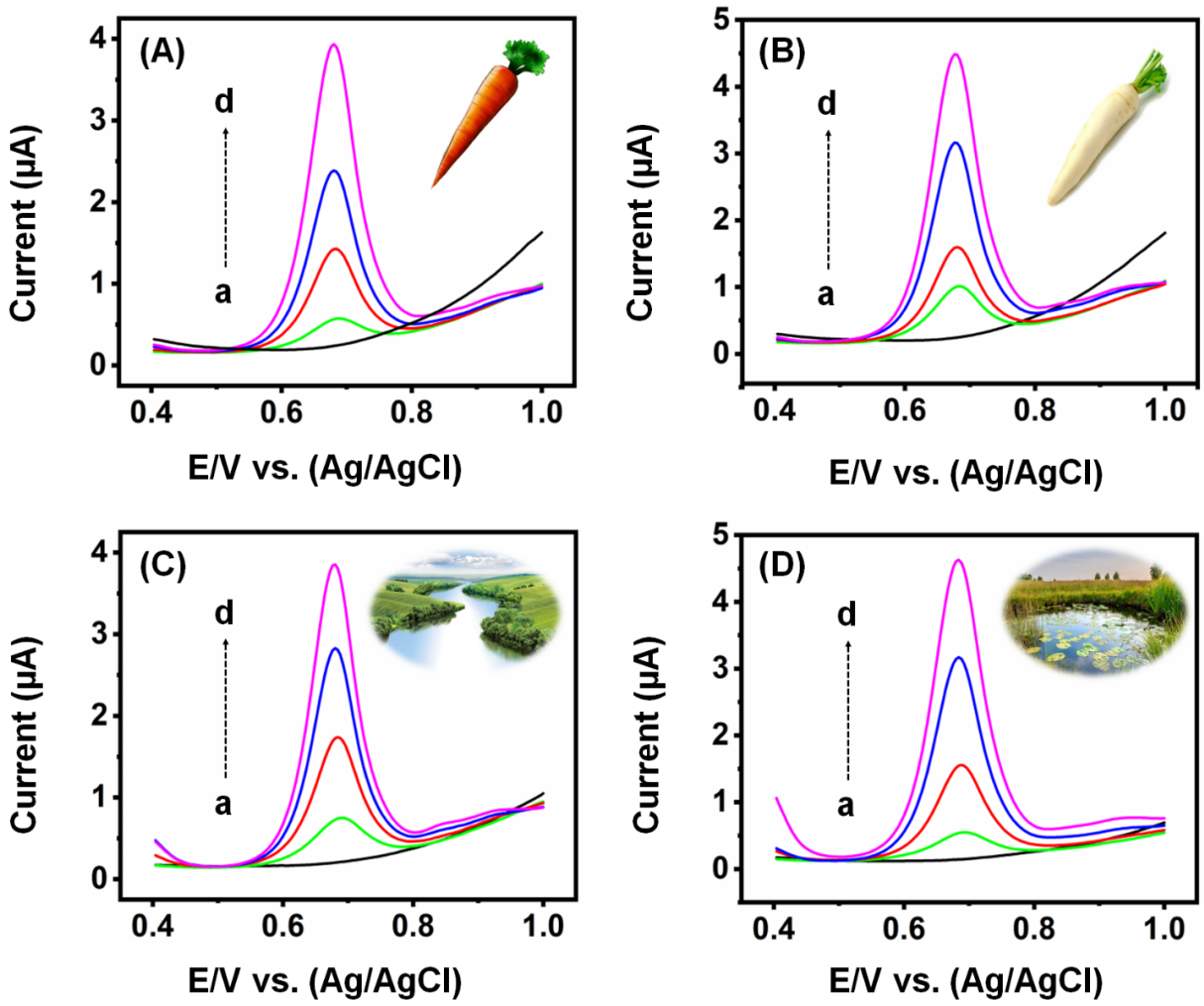

Fig. 8. DPV response of CBZ for the addition of 5, 10, 15, and 20 μM at Yb_2O_3/*f*-CNF/GCE in different real-time samples of (A) carrot, (B) radish, (C) lake water, and (D) pond water.

Table 2. Real-time determination of CBZ in food and water sample.

Sample	Added (μM)	Found (μM)	Recovery	RSD (%)
Carrot	5	4.80	96.07	1.00±1.69
	10	9.81	98.10	1.56±0.79
	15	14.66	97.79	3.19±2.32
	20	19.68	98.43	4.42±0.87
	5	3.85	96.49	0.56±1.45

Radish	10	9.79	97.91	1.40±2.35
	15	14.55	97.05	2.32±1.65
	20	19.79	98.98	3.88±1.39
Lake water	5	4.90	98.18	0.52±4.98
	10	9.61	98.08	1.51±3.97
	15	14.71	98.10	3.12±1.08
	20	19.78	98.92	4.57±1.26
Pond water	5	4.86	98.64	0.73±2.86
	10	9.94	99.42	1.72±0.72
	15	14.73	98.23	2.80±0.93
	20	19.75	98.70	3.81±0.86

5. Conclusion

S novel hybrid nanocomposite of Yb_2O_3/*f*-CNF has been prepared for the electrochemical detection of CBZ in vegetables and fruit samples. The morphological and structural characteristics of the developed Yb_2O_3/*f*-CNF nanocomposite were examined using various analytical and spectroscopic methods. The Yb_2O_3/*f*-CNF nanocomposite-modified GCE demonstrated a low LOD, a broad linear range, and relatively high sensitivity for the detection of CBZ. Additionally, the sensor exhibited high selectivity, stability, and anti-interference ability toward CBZ sensing, and showed satisfactory identification of CBZ in vegetables and water samples. The fabricated sensor could potentially be used to detect CBZ in real time.

Declaration of Competing Interest

The authors declare that they have no competing financial interests or personal relationships relevant to this paper.

Acknowledgements

451 The authors would like to thanks the National Taipei University of Technology, Yeungnam
452 University and Khalifa University for providing the necessary support for the study.

453

References

[1] R. Umapathi, S.M. Ghoreishian, S. Sonwal, G.M. Rani, Y.S. Huh, Portable electrochemical sensing methodologies for on-site detection of pesticide residues in fruits and vegetables, Coord. Chem. Rev. 453 (2022) 214305. https://doi.org/10.1016/j.ccr.2021.214305.

[2] P. Santhoshkumar, B. Thirumalraj, B. Sriram, K. Karuppasamy, D. Vikraman, A. Kathalingam, H. Choe, H.S. Kim, Mesoporous $SnSe_2$-grafted N-doped carbon composites with integrated flaky structure for electrochemical sensing of carbendazim, Ceram. Int. 48 (2022) 16023–16032. https://doi.org/10.1016/j.ceramint.2022.02.146.

[3] L. Wei, X. Huang, J. Yang, Y. Wang, K. Huang, L. Xie, F. Yan, L. Luo, C. Jiang, J. Liang, T. Li, Y. Ya, A high performance electrochemical sensor for carbendazim based on porous carbon with intrinsic defects, J. Electroanal. Chem. 915 (2022). https://doi.org/10.1016/j.jelechem.2022.116370.

[4] J.F. de Macedo, A.A.C. Alves, M.V.S. Sant'Anna, F.G.C. Cunha, G. de A.R. Oliveira, L.M. Lião, E.M. Sussuchi, Electrochemical determination of carbendazim in grapes and their derivatives by an ionic liquid-modified carbon paste electrode, J. Appl. Electrochem. 52 (2022) 729–742. https://doi.org/10.1007/s10800-021-01665-8.

[5] G. Peng, F. Gao, J. Zou, X. Wang, Y. Gao, H. Zhou, S. Liu, M. Li, L. Lu, One-step electrochemical synthesis of tremella-like Co-MOFs/carbon nanohorns films for enhanced electrochemical sensing of carbendazim in vegetable and fruit samples, J. Electroanal. Chem. 918 (2022) 116462. https://doi.org/10.1016/j.jelechem.2022.116462.

[6] M.L. Yola, Carbendazim imprinted electrochemical sensor based on $CdMoO_4$/g-C_3N_4 nanocomposite: Application to fruit juice samples, Chemosphere. 301 (2022) 134766.

https://doi.org/10.1016/j.chemosphere.2022.134766.

[7] L. Wei, X. Huang, J. Yang, Y. Wang, K. Huang, L. Xie, F. Yan, L. Luo, C. Jiang, J. Liang, T. Li, Y. Ya, A high performance electrochemical sensor for carbendazim based on porous carbon with intrinsic defects, J. Electroanal. Chem. 915 (2022). https://doi.org/10.1016/j.jelechem.2022.116370.

[8] G.A. Fozing Mekeuo, C. Despas, C. Péguy Nanseu-Njiki, A. Walcarius, E. Ngameni, Preparation of Functionalized Ayous Sawdust-carbon Nanotubes Composite for the Electrochemical Determination of Carbendazim Pesticide, Electroanalysis. 34 (2022) 667–676. https://doi.org/10.1002/elan.202100262.

[9] R. Liu, B. Li, F. Li, V. Dubovyk, Y. Chang, D. Li, K. Ding, Q. Ran, G. Wang, H. Zhao, A novel electrochemical sensor based on β-cyclodextrin functionalized carbon nanosheets@carbon nanotubes for sensitive detection of bactericide carbendazim in apple juice, Food Chem. 384 (2022). https://doi.org/10.1016/j.foodchem.2022.132573.

[10] H. Mahmoudi-Moghaddam, H. Akbari Javar, Z. Garkani-Nejad, Fabrication of platinum-doped $NiCo_2O_4$ nanograss modified electrode for determination of carbendazim, Food Chem. 383 (2022) 132398. https://doi.org/10.1016/j.foodchem.2022.132398.

[11] R. Elshafey, G.F. Abo-Sobehy, A.E. Radi, Imprinted polypyrrole recognition film @cobalt oxide/electrochemically reduced graphene oxide nanocomposite for carbendazim sensing, J. Appl. Electrochem. 52 (2022) 45–53. https://doi.org/10.1007/s10800-021-01613-6.

[12] Y. Li, Y. Feng, S. Chen, R. Li, Y. Yang, G. Bang, C. Ye, Signal on – off ratiometric electrochemical sensor coupled with a molecularly imprinted polymer for the detection of carbendazim, Microchim. Acta. (2022) 1–9. https://doi.org/10.1007/s00604-022-05341-2.

[13] R. Fu, J. Zhou, Y. Liu, Y. Wang, H. Liu, J. Pang, Y. Cui, Q. Zhao, C. Wang, Z. Li, B. Jiao, Y. He, Portable and quantitative detection of carbendazim based on the readout of a thermometer, Food Chem. 351 (2021). https://doi.org/10.1016/j.foodchem.2021.129292.

[14] Y. Li, Y. Feng, S. Chen, R. Li, Y. Yang, J. jing Guan, B.C. Ye, Signal on–off ratiometric electrochemical sensor coupled with a molecularly imprinted polymer for the detection of carbendazim, Microchim. Acta. 189 (2022) 1–9. https://doi.org/10.1007/s00604-022-05341-2.

[15] A. Yamuna, T.W. Chen, S.M. Chen, Synthesis and characterizations of iron antimony oxide nanoparticles and its applications in electrochemical detection of carbendazim in apple juice and paddy water samples, Food Chem. 373 (2022) 131569. https://doi.org/10.1016/j.foodchem.2021.131569.

[16] F. Beigmoradi, M. Rohani Moghadam, A. Bazmandegan-Shamili, H.R. Masoodi, Electrochemical sensor based on molecularly imprinted polymer coating on metal–organic frameworks for the selective and sensitive determination of carbendazim, Microchem. J. 179 (2022) 107633. https://doi.org/10.1016/j.microc.2022.107633.

[17] A.T. Ezhil Vilian, S.K. Hwang, M.J. Lee, Y.S. Huh, Y.K. Han, Manganese-doped zinc sulfide microspheres for improved electrocatalytic sensing ability toward carbendazim in food samples, Microchem. J. 175 (2022) 107204. https://doi.org/10.1016/j.microc.2022.107204.

[18] A. Sinha, Y. Huang, H. Zhao, Preparation of 3D assembly of mono layered molybdenum disulfide nanotubules for rapid screening of carbamate pesticide diethofencarb, Talanta. 204 (2019) 455–464. https://doi.org/10.1016/j.talanta.2019.06.040.

[19] A. Sinha, Dhanjai, R. Jain, H. Zhao, P. Karolia, N. Jadon, Voltammetric sensing based on the use of advanced carbonaceous nanomaterials: a review, Microchim. Acta. 185 (2018). https://doi.org/10.1007/s00604-017-2626-0.

[20] A. Sinha, Y. Huang, Dhanjai, K. Ma, H. Zhao, Electrochemical Oxidation of Tannic Acid at ZIF-8 Induced Nitrogen Doped Porous Carbon Nanoframework Modified Electrode, J. Electrochem. Soc. 165 (2018) H1004–H1011. https://doi.org/10.1149/2.1321814jes.

[21] F. Beigmoradi, M. Rohani Moghadam, A. Bazmandegan-Shamili, H. Reza Masoodi, Electrochemical sensor based on molecularly imprinted polymer coating on metal-organic frameworks for the selective and sensitive determination of carbendazim, Microchem. J. 179 (2022) 107633. https://doi.org/10.1016/j.microc.2022.107633.

[22] R. Liu, Y. Chang, F. Li, V. Dubovyk, D. Li, Q. Ran, H. Zhao, Highly sensitive detection of carbendazim in juices based on mung bean-derived porous carbon@chitosan composite modified electrochemical sensor, Food Chem. 392 (2022) 133301. https://doi.org/10.1016/j.foodchem.2022.133301.

[23] G. Peng, F. Gao, J. Zou, X. Wang, Y. Gao, H. Zhou, S. Liu, M. Li, L. Lu, One-step electrochemical synthesis of tremella-like Co-MOFs/carbon nanohorns films for enhanced electrochemical sensing of carbendazim in vegetable and fruit samples, J. Electroanal. Chem. 918 (2022) 116462. https://doi.org/10.1016/j.jelechem.2022.116462.

[24] M. Chen, Z. Zhao, X. Lan, Y. Chen, L. Zhang, R. Ji, L. Wang, Determination of carbendazim and metiram pesticides residues in reapeseed and peanut oils by fluorescence spectrophotometry, Meas. J. Int. Meas. Confed. 73 (2015) 313–317. https://doi.org/10.1016/j.measurement.2015.05.006.

[25] K. Yogesh Kumar, M.K. Prashanth, L. Parashuram, B. Palanivel, F.A. Alharti, B.H. Jeon, M.S. Raghu, Gadolinium sesquisulfide anchored N-doped reduced graphene oxide for sensitive detection and degradation of carbendazim, Chemosphere. 296 (2022) 134030. https://doi.org/10.1016/j.chemosphere.2022.134030.

[26] L. Wang, S.A. Haruna, W. Ahmad, J. Wu, Q. Chen, Q. Ouyang, Tunable multiplexed fluorescence biosensing platform for simultaneous and selective detection of paraquat and carbendazim pesticides, Food Chem. 388 (2022) 132950. https://doi.org/10.1016/j.foodchem.2022.132950.

[27] W. Zhong, F. Gao, J. Zou, S. Liu, M. Li, Y. Gao, Y. Yu, X. Wang, L. Lu, MXene@Ag-based ratiometric electrochemical sensing strategy for effective detection of carbendazim in vegetable samples, Food Chem. 360 (2021) 130006. https://doi.org/10.1016/j.foodchem.2021.130006.

[28] A. Özcan, F. Hamid, A.A. Özcan, Synthesizing of a nanocomposite based on the formation of silver nanoparticles on fumed silica to develop an electrochemical sensor for carbendazim detection, Talanta. 222 (2021). https://doi.org/10.1016/j.talanta.2020.121591.

[29] J.X. Man, J.T. Hu, D.K. Wang, S.J. He, Z.H. Lu, Ytterbium oxide electron injection interface in organic light-emitting diode, Appl. Phys. Lett. 120 (2022). https://doi.org/10.1063/5.0084140.

[30] V. Muthulakshmi, M. Sundrarajan, Green synthesis of ionic liquid assisted ytterbium oxide nanoparticles by Couroupita guianensis abul leaves extract for biological applications, J. Environ. Chem. Eng. 8 (2020) 103992. https://doi.org/10.1016/j.jece.2020.103992.

[31] F. Farbod, M. Mazloum-Ardakani, H.R. Naderi, H. Mohammadian-Sarcheshmeh, Synthesis

of a porous interconnected nitrogen-doped graphene aerogel matrix incorporated with ytterbium oxide nanoparticles and its application in superior symmetric supercapacitors, Electrochim. Acta. 306 (2019) 480–488. https://doi.org/10.1016/j.electacta.2019.03.131.

[32] M. Mazloum-Ardakani, A.A. Kalantari, Z. Alizadeh, H. Mohammadian-Sarcheshmeh, H. Banitaba, Electrochemical Investigation for Sensitive Determination of Metoclopramide Based on Ytterbium Oxide Nanoparticles Supported on Graphene, Anal. Bioanal. Chem. Res. 9 (2022) 299–307. https://doi.org/10.22036/abcr.2021.300086.1671.

[33] H.R. Naderi, M.R. Ganjali, A.S. Dezfuli, P. Norouzi, Sonochemical preparation of a ytterbium oxide/reduced graphene oxide nanocomposite for supercapacitors with enhanced capacitive performance, RSC Adv. 6 (2016) 51211–51220. https://doi.org/10.1039/c6ra02943d.

[34] A.A. Ibrahim, R. Ahmad, A. Umar, M.S. Al-Assiri, A.E. Al-Salami, R. Kumar, S.G. Ansari, S. Baskoutas, Two-dimensional ytterbium oxide nanodisks based biosensor for selective detection of urea, Biosens. Bioelectron. 98 (2017) 254–260. https://doi.org/10.1016/j.bios.2017.06.015.

[35] S. Ohmi, C. Kobayashi, I. Kashiwagi, C. Ohshima, H. Ishiwara, H. Iwai, Characterization of La_2O_3 and Yb_2O_3 Thin Films for High-k Gate Insulator Application, J. Electrochem. Soc. 150 (2003) F134. https://doi.org/10.1149/1.1581278.

[36] Y. Sohn, Yb_2O_3 nanowires, nanorods and nano-square plates, Ceram. Int. 44 (2018) 3341–3347. https://doi.org/10.1016/j.ceramint.2017.11.118.

[37] J. Yang, J. Shen, Q. Huang, Y. Guan, J. Miao, Hydrothermal synthesis and photoluminescence of host sensitized Yb_2O_3: Ho^{3+} nanorods, Mater. Res. Express. 6 (2019)

3–9. https://doi.org/10.1088/2053-1591/aae75d.

[38] M.C. Paul, B.N. Upadhyaya, S. Das, A. Dhar, M. Pal, S. Kher, K. Dasgupta, S.K. Bhadra, R. Sen, Study of the fabrication parameters of large core Yb_2O_3 doped optical fibre through solution doping technique, Opt. Commun. 283 (2010) 1039–1046. https://doi.org/10.1016/j.optcom.2009.06.006.

[39] T. Liu, X. Bai, C. Miao, Q. Dai, W. Xu, Y. Yu, Q. Chen, H. Song, Yb2O3/Au upconversion nanocomposites with broad-band excitation for solar cells, J. Phys. Chem. C. 118 (2014) 2908–2918. https://doi.org/10.1021/jp409581n.

[40] F. Unal, F. Kaya, Modelling of relation between synthesis parameters and average crystallite size of Yb_2O_3 nanoparticles using Box-Behnken design, Ceram. Int. 46 (2020) 26800–26808. https://doi.org/10.1016/j.ceramint.2020.07.155.

[41] M.S. Henriques, A.C. Ferreira, A. Cruz, L.M. Ferreira, J.B. Branco, P. Brázda, K. Jurek, T. Stora, A.P. Gonçalves, Preparation of Yb_2O_3 submicron-and nanomaterials via electrospinning, Ceram. Int. 41 (2015) 10795–10802. https://doi.org/10.1016/j.ceramint.2015.05.017.

[42] S. Kumar, G. Ram Chaudhary, S. Chaudhary, Designing of surface engineered Ytterbium oxide nanoparticles as effective electrochemical sensing platform for dopamine, J. Mol. Liq. 355 (2022) 118929. https://doi.org/10.1016/j.molliq.2022.118929.

[43] S. Hu, Q. Huang, Y. Lin, C. Wei, H. Zhang, W. Zhang, Z. Guo, X. Bao, J. Shi, A. Hao, Reduced graphene oxide-carbon dots composite as an enhanced material for electrochemical determination of dopamine, Electrochim. Acta. 130 (2014) 805–809. https://doi.org/10.1016/j.electacta.2014.02.150.

608 [44] B. Jiang, W. Yang, H. Bai, C. Wang, C. Xu, Z. Li, L. Yan, C. Zhang, N. Wu, S. Che, X.
609 Wang, Y. Li, Facile fabrication of Fe/Fe5C2@N-doped porous carbon as an efficient
610 microwave absorbent with strong and broadband absorption properties at an ultralow filler
611 loading, Carbon N. Y. 196 (2022) 890–901. https://doi.org/10.1016/j.carbon.2022.05.045.

612 [45] S. Ramki, R. Sukanya, S.M. Chen, M. Sakthivel, Y.T. Ye, Electrochemical detection of
613 toxic anti-scald agent diphenylamine using oxidized carbon nanofiber encapsulated
614 titanium carbide electrocatalyst, J. Hazard. Mater. 368 (2019) 760–770.
615 https://doi.org/10.1016/j.jhazmat.2019.01.110.

616 [46] M. Sakthivel, S. Ramaraj, S.M. Chen, B. Dinesh, H.V. Ramasamy, Y.S. Lee, Entrapment
617 of bimetallic $CoFeSe_2$ nanosphere on functionalized carbon nanofiber for selective and
618 sensitive electrochemical detection of caffeic acid in wine samples, Anal. Chim. Acta. 1006
619 (2018) 22–32. https://doi.org/10.1016/j.aca.2017.12.044.

620 [47] A.S. Haidyrah, P. Sundaresan, K. Venkatesh, S.K. Ramaraj, B. Thirumalraj, Fabrication of
621 functionalized carbon nanofibers/carbon black composite for electrochemical investigation
622 of antibacterial drug nitrofurantoin, Colloids Surfaces A Physicochem. Eng. Asp. 627
623 (2021) 127112. https://doi.org/10.1016/j.colsurfa.2021.127112.

624 [48] I.J.D. Priscillal, S.F. Wang, Coral reef-like zinc niobate nanostructures decorated
625 functionalized carbon nanofiber as electrode modifier for detection of oxidative stress
626 biomarker: 3-nitro-L-tyrosine, Mater. Today Chem. 25 (2022) 100970.
627 https://doi.org/10.1016/j.mtchem.2022.100970.

628 [49] A.S. Haidyrah, P. Sundaresan, K. Venkatesh, S.K. Ramaraj, B. Thirumalraj, Fabrication of
629 functionalized carbon nanofibers/carbon black composite for electrochemical investigation

of antibacterial drug nitrofurantoin, Colloids Surfaces A Physicochem. Eng. Asp. 627 (2021) 127112. https://doi.org/10.1016/j.colsurfa.2021.127112.

[50] T. Sakthi Priya, N. Nataraj, T.W. Chen, S.M. Chen, T. Kokulnathan, Synergistic formation of samarium oxide/graphene nanocomposite: A functional electrocatalyst for carbendazim detection, Chemosphere. 307 (2022) 135711. https://doi.org/10.1016/j.chemosphere.2022.135711.

[51] A. Şenocak, A. Khataee, E. Demirbas, E. Doustkhah, Ultrasensitive detection of rutin antioxidant through a magnetic micro-mesoporous graphitized carbon wrapped Co nanoarchitecture, Sensors Actuators, B Chem. 312 (2020). https://doi.org/10.1016/j.snb.2020.127939.

[52] R. Nehru, C. Di Dong, C.W. Chen, T.B. Nguyen, M.F. Li, Green and low-cost synthesis of yttrium oxide/graphene oxide binary sheets as a highly efficient electrocatalyst for voltammetric determination of 3-nitro-L-tyrosine, Colloids Surfaces A Physicochem. Eng. Asp. 635 (2022) 128089. https://doi.org/10.1016/j.colsurfa.2021.128089.

[53] C. Martínez-Sánchez, F. Montiel-González, V. Rodríguez-González, Electrochemical sensing of acetaminophen using a practical carbon paste electrode modified with a graphene oxide-Y_2O_3 nanocomposite, J. Taiwan Inst. Chem. Eng. 96 (2019) 382–389. https://doi.org/10.1016/j.jtice.2018.12.004.

[54] S. Chaudhary, S. Kumar, G.R. Chaudhary, Tuning of structural, optical and toxicological properties of Gd^{3+} doped Yb_2O_3 nanoparticles, Ceram. Int. 45 (2019) 19307–19315. https://doi.org/10.1016/j.ceramint.2019.06.181.

[55] S. Kalaiarasi, M. Kavitha, P. Karpagavinayagam, C. Vedhi, R.R. Muthuchudarkodi,

652 Materials Today : Proceedings Tungsten oxide decorated graphene oxide nanocomposite :
653 Chemical synthesis , characterization and application in super capacitors, Mater. Today
654 Proc. 48 (2022) 282–289. https://doi.org/10.1016/j.matpr.2020.07.207.

655 [56] R.R. Nallapureddy, M.R. Pallavolu, S.W. Joo, Construction of Functionalized Carbon
656 Nanofiber-g-C_3N_4 and TiO_2 Spheres as a Nanostructured Hybrid Electrode for High-
657 Performance Supercapacitors, Energy and Fuels. 35 (2021) 1796–1809.
658 https://doi.org/10.1021/acs.energyfuels.0c03545.

659 [57] V. Muthulakshmi, P. Kumar, M. Sundrarajan, Journal of Environmental Chemical
660 Engineering Green synthesis of Ionic liquid mediated Ytterbium oxide nanoparticles by A
661 ndrographis Paniculata leaves extract for structural , morphological and biomedical
662 applications, J. Environ. Chem. Eng. 9 (2021) 105270.
663 https://doi.org/10.1016/j.jece.2021.105270.

664 [58] S. Kumar, H. Tripathi, J. Sharma, U. Batra, Structural, morphological, and opto-electrical
665 properties of $Y_{2-x}Yb_xO_3$ nanoparticles synthesized using coprecipitation method, Int. J.
666 Appl. Ceram. Technol. 18 (2021) 12–23. https://doi.org/10.1111/ijac.13603.

667 [59] R.R. Pasupuleti, P.C. Tsai, V.K. Ponnusamy, Low-cost disposable Poly(ethyleneimine)-
668 Functionalized Carbon Nanofibers Coated Cellulose Paper as efficient solid phase
669 extraction sorbent material for the extraction of Parahydroxybenzoates from environmental
670 waters, Chemosphere. 267 (2021) 129274.
671 https://doi.org/10.1016/j.chemosphere.2020.129274.

672 [60] K. Du, X. Xu, S. Yao, P. Lei, L. Dong, M. Zhang, J. Feng, H. Zhang, Enhanced
673 upconversion luminescence and controllable phase/shape of NaYF4:Yb/Er crystals through

674 Cu^{2+} ion doping, CrystEngComm. 20 (2018) 1945–1953.
675 https://doi.org/10.1039/c7ce02227a.

676 [61] S.C. Sarma, U. Subbarao, Y. Khulbe, R. Jana, S.C. Peter, Are we underrating rare earths as
677 an electrocatalyst? the effect of their substitution in palladium nanoparticles enhances the
678 activity towards ethanol oxidation reaction, J. Mater. Chem. A. 5 (2017) 23369–23381.
679 https://doi.org/10.1039/c7ta07945a.

680 [62] Y. Liang, Y. Wang, H. Mi, L. Sun, D. Ma, H. Li, C. He, P. Zhang, Functionalized carbon
681 nanofiber interlayer towards dendrite-free, Zn-ion batteries, Chem. Eng. J. 425 (2021)
682 131862. https://doi.org/10.1016/j.cej.2021.131862.

683 [63] T.F. Yi, H. Chang, T.T. Wei, S.Y. Qi, Y. Li, Y.R. Zhu, Approaching high-performance
684 electrode materials of $ZnCo_2S_4$ nanoparticle wrapped carbon nanotubes for supercapacitors,
685 J. Mater. 7 (2021) 563–576. https://doi.org/10.1016/j.jmat.2020.11.015.

686 [64] Q. Wu, H. Bai, A. Gao, J. Zhu, High-density grafting of carbon nanotube/carbon nanofiber
687 hybrid on carbon fiber surface by vacuum filtration for effective interfacial reinforcement
688 of its epoxy composites, Compos. Sci. Technol. 225 (2022) 109522.
689 https://doi.org/10.1016/j.compscitech.2022.109522.

690 [65] D. Kong, X. Li, Y. Tang, M. Sui, J. Li, Y. Ma, G. Wang, W. Gu, X. Guo, M. Yang, A highly
691 parallel DTT/MB-DNA/Au electrochemical biosensor for trace Hg monitoring by using
692 configuration occupation approach and SECM, Ecotoxicol. Environ. Saf. 234 (2022)
693 113391. https://doi.org/10.1016/j.ecoenv.2022.113391.

694 [66] Q. Li, C. Huo, K. Yi, L. Zhou, L. Su, X. Hou, Preparation of flake hexagonal BN and its
695 application in electrochemical detection of ascorbic acid , dopamine and uric acid, Sensors

Actuators B. Chem. 260 (2018) 346–356. https://doi.org/10.1016/j.snb.2017.12.208.

[67] J. Feng, Q. Li, J. Cai, T. Yang, J. Chen, X. Hou, Sensors and Actuators B : Chemical Electrochemical detection mechanism of dopamine and uric acid on titanium nitride-reduced graphene oxide composite with and without ascorbic acid, Sensors Actuators B. Chem. 298 (2019) 126872. https://doi.org/10.1016/j.snb.2019.126872.

[68] Y. Xue, Y. Zheng, E. Wang, T. Yang, H. Wang, X. Hou, $Ti_3C_2T_x$ (MXene)/ Pt nanoparticle electrode for the accurate detection of DA coexisting with AA and UA, Dalton Trans., (2022) 4549–4559. https://doi.org/10.1039/d2dt00110a.

[69] Y. Xie, F. Gao, X. Tu, X. Ma, R. Dai, G. Peng, Y. Yu, L. Lu, Flake-like neodymium molybdate wrapped with multi-walled carbon nanotubes as an effective electrode material for sensitive electrochemical detection of carbendazim, J. Electroanal. Chem. 855 (2019) 113468. https://doi.org/10.1016/j.jelechem.2019.113468.

[70] I. Suresh, S. Selvaraj, N. Nesakumar, J.B.B. Rayappan, A.J. Kulandaiswamy, Nanomaterials based non-enzymatic electrochemical and optical sensors for the detection of carbendazim: A review, Trends Environ. Anal. Chem. 31 (2021) e00137. https://doi.org/10.1016/j.teac.2021.e00137.

[71] Y. Dong, L. Yang, L. Zhang, Simultaneous electrochemical detection of benzimidazole fungicides carbendazim and thiabendazole using a novel nanohybrid material-modified electrode, J. Agric. Food Chem. 65 (2017) 727–736. https://doi.org/10.1021/acs.jafc.6b04675.

[72] C.A. Razzino, L.F. Sgobbi, T.C. Canevari, J. Cancino, S.A.S. Machado, Sensitive determination of carbendazim in orange juice by electrode modified with hybrid material,

718 Food Chem. 170 (2015) 360–365. https://doi.org/10.1016/j.foodchem.2014.08.085.

719 [73] D. Wu, M. Wu, J. Yang, H. Zhang, K. Xie, C. Te Lin, A. Yu, J. Yu, L. Fu, Delaminated
720 $Ti_3C_2T_x$ (MXene) for electrochemical carbendazim sensing, Mater. Lett. 236 (2019) 412–
721 415. https://doi.org/10.1016/j.matlet.2018.10.150.

722 [74] R. Cui, D. Xu, X. Xie, Y. Yi, Y. Quan, M. Zhou, J. Gong, Z. Han, G. Zhang, Phosphorus-
723 doped helical carbon nanofibers as enhanced sensing platform for electrochemical detection
724 of carbendazim, Food Chem. 221 (2017) 457–463.
725 https://doi.org/10.1016/j.foodchem.2016.10.094.

726 [75] C. Tian, S. Zhang, H. Wang, C. Chen, Z. Han, M. Chen, Y. Zhu, R. Cui, G. Zhang, Three-
727 dimensional nanoporous copper and reduced graphene oxide composites as enhanced
728 sensing platform for electrochemical detection of carbendazim, J. Electroanal. Chem. 847
729 (2019) 113243. https://doi.org/10.1016/j.jelechem.2019.113243.

730 [76] Y. Zhou, Y. Li, P. Han, Y. Dang, M. Zhu, Q. Li, Y. Fu, A novel low-dimensional heteroatom
731 doped Nd_2O_3 nanostructure for enhanced electrochemical sensing of carbendazim, New J.
732 Chem. 43 (2019) 14009–14019. https://doi.org/10.1039/c9nj02778e.

733 [77] Y. Zhou, R. Cui, Y. Dang, Y. Li, Y. Zou, Doping controlled oxygen vacancies of $ZnWO_4$
734 as a novel and effective sensing platform for carbendazim and biomolecule, Sensors
735 Actuators, B Chem. 296 (2019) 126680. https://doi.org/10.1016/j.snb.2019.126680.

736 [78] D. Ilager, H. Seo, S.S. Kalanur, N.P. Shetti, T.M. Aminabhavi, A novel sensor based on
737 WO3·0.33H2O nanorods modified electrode for the detection and degradation of herbicide,
738 carbendazim, J. Environ. Manage. 279 (2021) 111611.
739 https://doi.org/10.1016/j.jenvman.2020.111611.

[79] A. Yamuna, T.W. Chen, S.M. Chen, T.Y. Jiang, Facile synthesis of single-crystalline Fe-doped copper vanadate nanoparticles for the voltammetric monitoring of lethal hazardous fungicide carbendazim, Microchim. Acta. 188 (2021). https://doi.org/10.1007/s00604-021-04941-8.

[80] P.C.A. Santana, J.B.S. Lima, T.B.S. Santana, L.F.S. Santos, C.R.S. Matos, L.P. da Costa, I.F. Gimenez, E.M. Sussuchi, Semiconductor nanocrystals-reduced graphene composites for the electrochemical detection of carbendazim, J. Braz. Chem. Soc. 30 (2019) 1302–1308. https://doi.org/10.21577/0103-5053.20190026.

[81] A.M. Ashrafi, J. Dordević, V. Guzsvány, I. Švancara, T. Trtić-Petrović, M. Purenović, K. Vytřas, Trace determination of Carbendazim fungicide using adsorptive stripping voltammetry with a carbon paste electrode containing tricresyl phosphate, Int. J. Electrochem. Sci. 7 (2012) 9717–9731.

[82] W.F. Ribeiro, T.M.G. Selva, I.C. Lopes, E.C.S. Coelho, S.G. Lemos, F. Caxico De Abreu, V. Bernardo Do Nascimento, M.C. Ugulino De Araújo, Electroanalytical determination of carbendazim by square wave adsorptive stripping voltammetry with a multiwalled carbon nanotubes modified electrode, Anal. Methods. 3 (2011) 1202–1206. https://doi.org/10.1039/c0ay00723d.